Chemical Engineering Science 191 (2018) 232–244

Contents lists available at ScienceDirect

Chemical Engineering Science

journal homepage: www.elsevier.com/locate/ces

Protein crystallization in a droplet-based microfluidic device: Hydrodynamic analysis and study of the phase behaviour

J. Ferreira [a,b], F. Castro [b,c], F. Rocha [b,*], S. Kuhn [a,*]

[a] Department of Chemical Engineering, KU Leuven, Leuven, Belgium
[b] LEPABE – Laboratory for Process Engineering, Biotechnology & Energy, Department of Chemical Engineering, Faculty of Engineering of the University of Porto, Porto, Portugal
[c] CEB – Centre of Biological Engineering, Department of Biological Engineering, University of Minho, Braga, Portugal

HIGHLIGHTS

- Systematic study of protein phase behaviour in a droplet-based microreactor.
- Numerical prediction of droplet sizes in a flow-focusing geometry.
- Parametric study to quantify the influence of the droplet volume on nucleation.
- Parametric study of the influence of the droplet volume on the phase diagram limits.

GRAPHICAL ABSTRACT

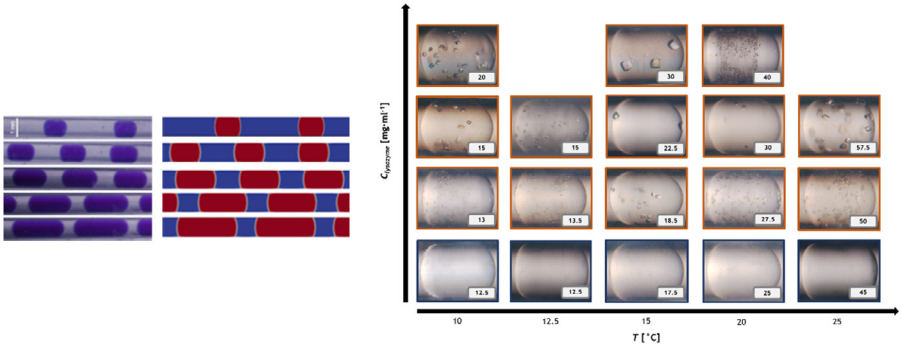

ARTICLE INFO

Article history:
Received 24 April 2018
Received in revised form 12 June 2018
Accepted 24 June 2018
Available online 25 June 2018

Keywords:
Protein crystallization
Droplet-based microfluidics
Phase diagram
Nucleation

ABSTRACT

This work reports a cheap and easy-to-use droplet-based microfluidic platform for the study of protein crystallization, offering the possibility to characterize the protein phase behaviour, and the effect of volumetric and interfacial phenomena on the crystallization mechanism. We conducted a parametric study supported by comparison with literature data, to quantify the influence of the droplet volume on the thermodynamic (solubility data) and kinetic (metastability data) parameters, using lysozyme as a model protein. Experiments were performed in a tubular microreactor at low Capillary numbers (4.1×10^{-5}–2.3×10^{-4}), resulting in a broad range of droplet sizes. The droplet formation in a flow-focusing geometry was also numerically studied using CFD and a correlation for the droplet size was developed. Subsequently, the lysozyme phase behaviour and the possible mechanisms associated with the nucleation process were evaluated. While crystallization in small volume droplets is usually characterized by a low nucleation probability and correspondingly low number of crystals, we did not observe this in our experiments. A potential explanation for this is the complex and stochastic mechanism of nucleation, including the competition between monomers and oligomers in solution.

1. Introduction

Since the pioneering work of Friedrich Hünefeld in 1840, who accidentally discovered protein crystals in blood samples (Giegé, 2013), researchers from different scientific fields are trying to produce high-quality protein crystals for three dimensional (3D) structure determination by X-ray crystallography (Vorontsova et al., 2015; Leng and Salmon, 2009; Haeberle and Zengerle, 2007; Maeki et al., 2016; Yang et al., 2010; Shui et al., 2007; Teh et al., 2008). Proteins are the building blocks of all cells in all living organisms and their function is dependent on their structure,

* Corresponding authors.
E-mail addresses: frocha@fe.up.pt (F. Rocha), simon.kuhn@kuleuven.be (S. Kuhn).

https://doi.org/10.1016/j.ces.2018.06.066
0009-2509/

Nomenclature

Roman symbols

C	concentration [mol·m^{-3}]
Ca	Capillary number (Ca $= \mu u/\sigma$) [–]
Co	Courant number (Co $= \lvert\vec{u}\rvert\Delta t/\Delta x$) [–]
d	diameter [m]
Δt	time-step [s]
Δx	cell size [m]
d_t	Teflon tube diameter [m]
e	wall wetting film thickness [m]
f_σ	surface tension force [kg·m^{-2}·s^{-2}]
g	gravity acceleration [m·s^{-2}]
L	length [m]
$\hat{n}$	unit surface normal vector [–]
Q	flow rate [m^3·s^{-1}]
P	probability [–]
S	supersaturation [–]
T	temperature [K]
u	velocity [m·s^{-1}]
V	volume [m^3]

Greek symbols

μ	dynamic viscosity [Pa·s]
α	marker function (volume fraction) [–]
ρ	density [kg·m^{-3}]
σ	surface tension [N·m^{-1}]
κ	local surface curvature [–]
θ	contact angle [°]

Subscripts

c	continuous phase
d	dispersed phase
i	phase (i $=$ c, d)
nucl	nucleation
t	Teflon tube
0	initial

Abbreviations

CFD	Computational Fluid Dynamics
CFL	Courant-Friedrichs-Lewy
CSF	Continuum Surface Force
MULES	Multidimensional Universal Limiter with Explicit Solution
MZW	metastable zone width
OF	OpenFoam®
PFA	perfluoroalkoxy alkane
PIMPLE	Pressure Implicit Method for Pressure Linked Equations
VOF	Volume-of-Fluid method

therefore determining their 3D structure is of importance. This is a crucial insight for fundamental research in biochemistry for the identification and design of new drugs and pharmaceutical products, and to understand biological systems at a molecular level (Walsh, 2015). However, crystallization of proteins is a complex and multiparametric process, involving thermodynamic and kinetic features, as well as the optimization of several variables (*i.e.* temperature, pH, and concentrations of protein and precipitant agent, among others), where there is not an accurate theory to substitute for empirical approaches (Leng and Salmon, 2009; Yang et al., 2010).

Crystallization is a two-step physical process in which the supersaturation is the driving force. The first step (nucleation) is the formation of nuclei, followed by the growth of these nuclei to a macroscopic scale (crystal growth). Compared to crystal growth, nucleation is more difficult to address theoretically and experimentally due to its stochastic nature and the high supersaturation levels to overcome the critical activation free energy barrier (Vorontsova et al., 2015; Leng and Salmon, 2009; Haeberle and Zengerle, 2007; Maeki et al., 2016; Yang et al., 2010; Shui et al., 2007; Teh et al., 2008). Associated with the highly stochastic nature of protein nucleation, it is often a matter of trial-and-error to successfully crystallize a protein. This implies testing a large number of potential crystallization conditions with large amounts of protein of interest. Since proteins are usually only available in low quantities, high-throughput experimental methodologies for the acquisition of relevant thermodynamic and kinetic data, as well as more systematic crystallization strategies are needed. An example of a systematic strategy for monitoring nucleation and crystal growth is using seeding, which allows a better control of crystal size and the reduction of crystallization time (Leng and Salmon, 2009; Schieferstein et al., 2018; Gerdts et al., 2006; Revalor et al., 2010).

Crystallization processes can be situated in a phase diagram, which indicates which state (liquid, crystalline, or amorphous precipitate) is stable when varying crystallization parameters. Fig. 1 depicts the protein concentration as a function of adjustable parameters (e.g. precipitant agent concentration). In the labile zone (nucleation zone) the spontaneous formation of new nuclei is occurring, whereas in the metastable zone crystal growth is favoured, with a low probability for the formation of new nuclei. In addition, there is a stable zone (below the solubility curve), where the protein is soluble, and a precipitation zone, where the formation of an amorphous solid phase is observed (Chayen and Saridakis, 2008).

The information on protein phase behaviour is fundamental for a systematic design of crystallization experiments, which contributes to a more accurate prediction of protein crystallization conditions. However, most of the studies were focused on the solubility instead of the metastability data (Forsythe et al., 1999; Howard et al., 1988). The effect of different parameters on the metastability limit was reported in a few number of publications. For example, the effect of salt concentration was studied by Crespo et al. (2010) and Castro et al. (2016), the temperature effect

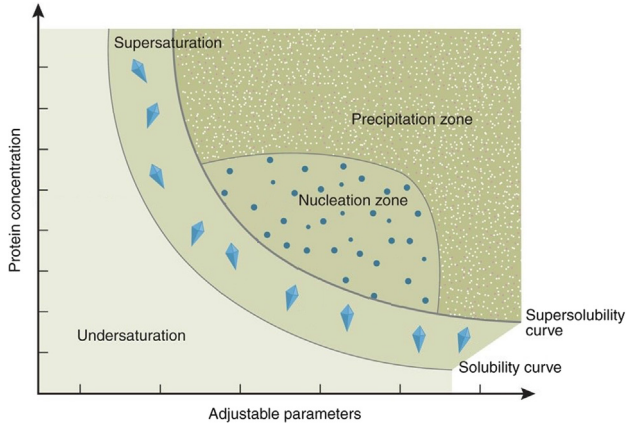

Fig. 1. Representation of the phase behaviour of a biological macromolecule: Stable (undersaturation), metastable (below the nucleation zone), nucleation and precipitation zones [Adapted from Chayen and Saridakis (2008)].

by Maosoongnern et al. (2012) and Ildefonso et al. (2012), and the ultrasound effect also by Crespo et al. (2010).

Protein crystallization in droplets has become an increasingly popular topic during the last decade. Droplet-based microfluidics represents an attractive tool for high-throughput screening experimentation (Maeki et al., 2016; Teh et al., 2008; Whitesides, 2006; Belkadi et al., 2015; Squires and Quake, 2005), since each droplet is considered as an independent microreactor, allowing to carry out a large number of experiments under identical conditions, offering thus more flexibility at minimal material consumption (Baroud et al., 2010). This segmented flow system creates discrete volumes using immiscible phases, where the droplets (dispersed phase) are generated within a second immiscible carrier fluid (continuous phase) along the microchannels (Günther and Jensen, 2006). The droplet breakup and size are determined by the hydrodynamic conditions (*i.e.* cross-flow, co-flow or flow-focusing) and the flow rates of the two fluids. These combined effects will determine the regime of droplet formation (Teh et al., 2008; Squires and Quake, 2005; Anna, 2016). Furthermore, droplet-based microfluidics provides unique experimental approaches when compared to larger scale systems, such as control of molecular diffusion and protein crystal nucleation (Li and Ismagilov, 2010). Different materials and designs of microfluidic devices have been reported for protein crystallization experiments (Gerdts et al., 2006; Ildefonso et al., 2012a, 2012b, 2011; Leng and Salmon, 2009; Haeberle and Zengerle, 2007; Maeki et al., 2016; Zheng et al., 2005, 2004; Dhouib et al., 2009; Hamon and Hong, 2013; Shi et al., 2017; Zhang et al., 2015a,b, 2017a,b; Yamaguchi et al., 2013; Hammadi et al., 2013). Numerical simulations can facilitate the design of microfluidic devices for protein crystallization experiments, as reported by Zhang et al. (2015a,b), Wang et al. (2013), Ngo et al. (2015), Li et al. (2014), and Wang et al. (2015). Furthermore, simulations of the droplet formation can be used to reduce the number of costly and time-consuming experiments. Different models have been proposed following Lagrangian (*i.e.* Moving Mesh and Front-Tracking) and Eulerian (*i.e.* Volume-of-Fluid, Level-Set and Phase Field) approaches with commercial and open source software (Wörner, 2012). Controlling the droplet volume is important to achieve a better understanding of the nucleation phenomenon (Hammadi et al., 2013; Grossier et al., 2011), which is not yet explored in detail. Only the works reported by Zhang et al. (2015a,b, 2017a,b), Hammadi et al. (2013), Roberts et al. (2010), and Akella et al. (2014) present contributions to justify the crucial influence of the droplet volume on protein crystallization.

In the present work, we study lysozyme phase behaviour at 3% (w/v) sodium chloride and pH 4.7 in a droplet-based microfluidic platform. This platform consists of a Teflon tube arranged in a serpentine shape and basic passive micromixers (*T*- and flow-focusing junctions). First, a hydrodynamic study in the squeezing flow regime, which allows a wide range of droplet sizes, was conducted for a range of low values of the Capillary number (Ca), using experimental and numerical approaches. The lysozyme phase diagram was then built for a single droplet size condition.

2. Materials and methods

2.1. Experimental methods

2.1.1. Experimental set-up

The developed droplet-based microfluidic platform consists of a Teflon tube (PFA tubing 1/16″ OD × 0.040″ ID × 5 ft, *IDEX Health & Science*) fixed by an acrylic plate and then jacketed to control the temperature through a water bath (*Huber – Ministat 125*, accuracy ± 0.02 °C). Syringe pumps (*NE-4000, New Era, USA*) were used to control the flow rates of both phases. Glass syringes (*Fortuna Optima® Ganzglasspritze, Poulten & Graf GmbH*) were used for improved flow rate control and avoiding pulsation (Zhang et al., 2017a,b).

The microfluidic platform was placed under an optical microscope (*Nikon SMZ1500 Stereoscopic Zoom Microscope* with a *Nikon DS-2M digital camera*) to measure the droplet sizes and monitor the nucleation events. Time-lapsing images were post-processed for further analysis (including the determination of the static contact angle) using the *NIS-Elements Basic Research Imaging software* ("NIS Elements Basic Research – Microscope Imaging Software", 2017). The characterization of the droplet size distribution was done using an image analysis methodology reported by Ferreira et al. (2011, 2012). The experimental set-up involves three main parts (A–C) as indicated in Fig. 2.

The fluid connections consist of a *T*-junction (Tee Tefzel 1/16″ 0.020″ thru-hole) for the mixing of the protein and the precipitant agent (NaCl) aqueous solutions, and a flow-focusing junction (Cross PEEK 1/16″ 0.020″ thru-hole), where the dispersed (crystallizing solution) and continuous phase (silicon oil, *Hampton Research™*) meet forming droplets. A preliminary numerical study was also conducted for choosing the contacting geometry, following the strategy discussed in the next subsection. The premixing at the *T*-junction was used to avoid nucleation in the glass syringes before starting the temperature control. The outlet junction was connected to a serpentine Teflon tube and the generated droplets were distributed continuously along its entire length (1.2 m).

2.1.2. Fluid flow segmentation

The physical properties of the studied liquids are listed in Table 1. Silicon oil is commonly used in crystallization experiments, due to its good wettability of Teflon surfaces. Therefore, it was possible to generate aqueous droplets avoiding contact with the Teflon wall, preventing possible protein adsorption by the microchannel surface and, at the same time, increasing the frequency of droplet generation. It was assumed that the protein and precipitant agent aqueous solutions were sufficiently diluted to neglect a concentration effect on the physical properties of the fluids. Dynamic viscosity and interfacial tension were measured using a rotational rheometer (*Physica MCR301, Anton Paar*) and an optical tensiometer (*Biolin Scientific Theta Lite 100*), respectively.

2.2. Numerical methodology

The Volume-of-Fluid (VOF) interface capturing approach was selected to predict the droplet formation in the flow-focusing geometry. The particular challenge of the numerical study is related to the low Capillary numbers (see Table 2), as this dominance of surface tension is known to introduce spurious currents in the solution (Lafaurie et al., 1994). For computations we used OpenFOAM-5.x (Weller, 2017) and the *interFoam* solver with the extension of the "interfaceProperties" library (van As, 2017), which was initially reported by Hoang et al. (2013). In the following section we briefly summarize the governing equations and the solution schemes (Kirby, 2010; Tabeling, 2005). Assuming incompressible flow and Newtonian fluids, the two-phase flow is governed by the conservation of mass (continuity equation)

$$\frac{\partial \rho}{\partial t} + \nabla \cdot (\rho \vec{u}) = 0 \tag{1}$$

where ρ is the fluid density [kg·m^{-3}], t the time [s], and $\vec{u}$ is the fluid velocity vector, and conservation of momentum (Navier-Stokes equations)

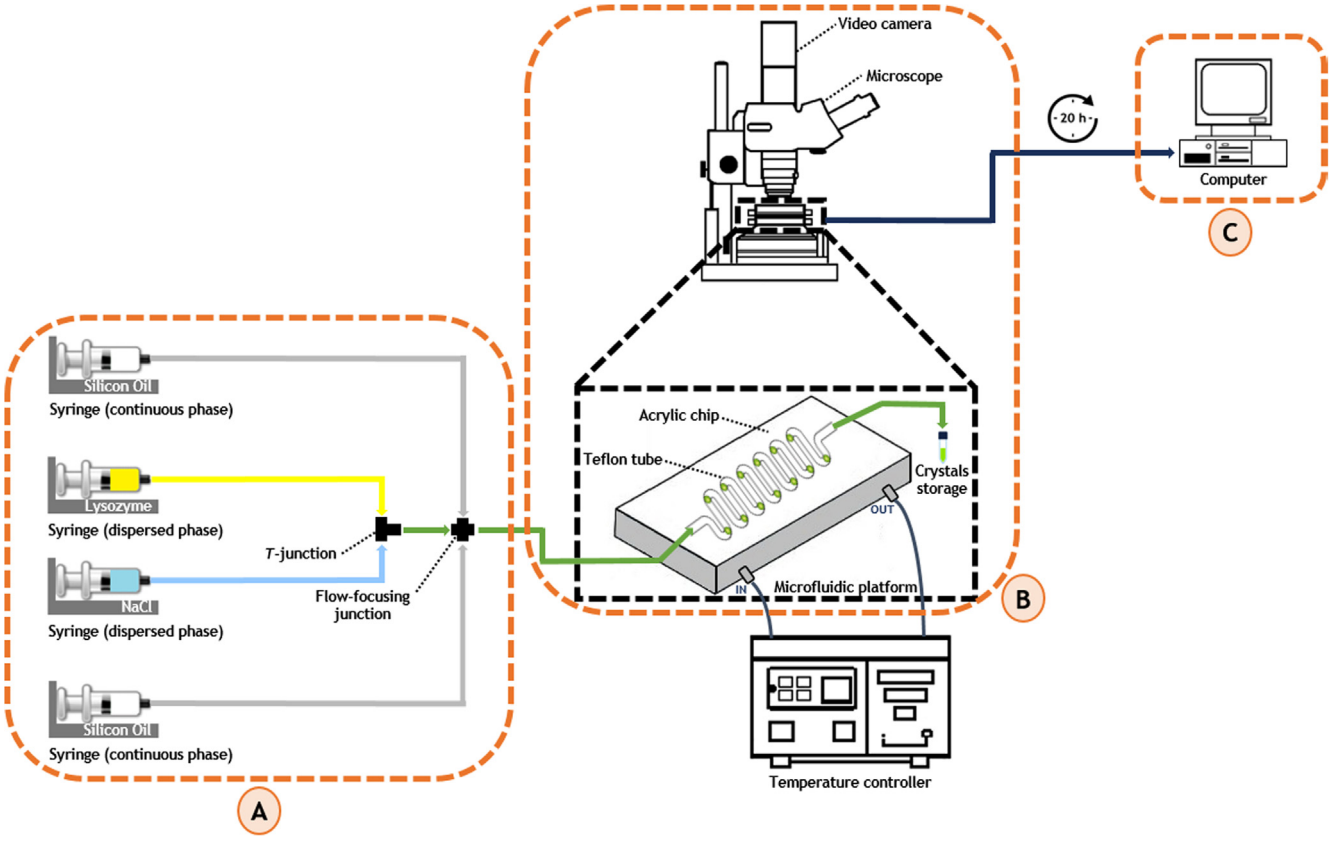

Fig. 2. Schematic overview of the experimental set-up: (A) Droplet production and detection: Injection of dispersed (*T*-junction) and continuous (flow-focusing junction) phases using syringe pumps; (B) Droplet incubation and observation: Microfluidic platform with an integrated temperature controller. Experiments are monitored by optical microscopy and the crystals are collected at the end of the reactor; (C) Data acquisition and analysis: Crystal counting and droplet size measurements by image analysis techniques.

Table 1
Physical properties of the fluids at T = 20 °C.

Fluid	Density, ρ [kg·m^{-3}]	Dynamic viscosity, μ [mPa·s]	Interfacial tension, σ [mN·m^{-1}]	Contact angle, θ [°]
Water (dispersed phase)	1000	1	38.74	120
Silicon oil (continuous phase)	827	0.95		

Table 2
Overview of the hydrodynamic points for the segmented flow regimes under study.

Regime	Droplet	Irregular segmented		Plug	
Case	#1	#2	#3	#4	#5
Q_c [ml·min^{-1}]	0.200	0.250	0.200	0.150	0.150
Q_d [ml·min^{-1}]	0.080	0.200	0.300	0.315	0.435
α_c	0.714	0.556	0.400	0.323	0.256
Ca_c	1.0×10^{-4}	1.3×10^{-4}	1.0×10^{-4}	7.8×10^{-5}	7.8×10^{-5}
Ca_d	4.1×10^{-5}	1.0×10^{-4}	1.5×10^{-4}	1.6×10^{-4}	2.3×10^{-4}
V_d [μl]	0.9	2.1	3.7	8.8	18.3
t_r [min]	11.4	4.6	3.0	2.9	2.1
f_d [s^{-1}]	1.4	2.4	2.9	2.0	1.9

[Note 1: Droplet frequency, f_d: $f_d = u_d/L_d$.]
[Note 2: Reactor residence time, $t_r = L_t/u_d$, where L_t and u_d define, respectively, length of Teflon tube and velocity of dispersed phase.]
[Note 3: Droplet volume, V_d (Nie et al., 2008): $V_d = \pi/12[2L_d^3 - (L_d - d_d)^2(2L_d + d_d)]$, where L_d and d_d represent the droplet length and the droplet diameter, respectively.]

$$\rho\left(\frac{\partial \vec{u}}{\partial t} + \vec{u}\cdot\nabla\vec{u}\right) = -\vec{\nabla p} + \mu\nabla^2\vec{u} + \rho\vec{g} + \vec{f_\sigma} \quad (2)$$

where μ is the dynamic viscosity [Pa·s] and g the gravitational acceleration [m·s^{-2}]; $\vec{\nabla p}$ represents the pressure forces, and $\vec{f_\sigma}$ the surface tension forces. The surface tension force is modelled as a volumetric force by the Continuum Surface Force (CSF) method (Brackbill et al., 1992).

$$\vec{f_\sigma} = \sigma\kappa\vec{n} \quad (3)$$

where σ is the interfacial tension, κ the interface curvature ($\kappa = \nabla\cdot\vec{n}$), and $\hat{n}$ the interface-normal vector $\left(\vec{n} = \frac{\nabla\alpha}{|\nabla\alpha|}\right)$. In

addition to the continuity and Navier-Stokes equations, the VOF method solves an advection equation for the phase indicator function (α).

$$\frac{\partial \alpha}{\partial t} + \nabla \cdot (\alpha \vec{u}) = 0 \tag{4}$$

where α varies from 0 to 1, with $\alpha = 1$ representing the dispersed phase, $\alpha = 0$ the continuous phase, and grid cells that contain the interface have a value situated between 0 and 1, depending on the volume fraction of each phase. The fluid properties are calculated according to Eqs. (5) and (6).

$$\rho = \alpha \rho_{\mathrm{d}} + (1 - \alpha)\rho_{\mathrm{c}} \tag{5}$$

$$\mu = \alpha \mu_{d} + (1 - \alpha)\mu_{c} \tag{6}$$

Due to the large gradients in the α field, the phase-fraction equation is penalized by numerical diffusion (Hoang et al., 2013). To counteract, Eq. (4) is extended with an interface compression term [3rd term in Eq. (7)] which is only active in the interface region (Nieves-Remacha et al., 2015).

$$\frac{\partial \alpha}{\partial t} + \nabla \cdot (\alpha \vec{u}) + \nabla \cdot [\vec{u_r} \alpha (1 - \alpha)] = 0 \tag{7}$$

Since the fluid interface is implicitly represented by the VOF function, the phase fraction variable is discrete, and abrupt changes in its value lead to errors in the calculation of the interface curvature and normal vectors. These errors can induce the appearance of artificial velocity magnitude values where the calculation of the interface forces is more difficult (e.g. regions near the droplet interface and on the recirculation zones inside the droplet). Hoang et al. (2013) proposed that if the curvature (κ) is computed from a smoothed VOF function ($\tilde{\alpha}$) over a finite region around the fluid interface, the appearance of non-physical spurious currents should be suppressed.

$$\kappa = \nabla \cdot \left(\frac{\nabla \tilde{\alpha}}{|\nabla \tilde{\alpha}|} \right) \tag{8}$$

A Laplacian filter was proposed by Lafaurie et al. (1994) and the transformation from the VOF function α to a smoother function $\tilde{\alpha}_k$ is done according to Eq. (9).

$$\tilde{\alpha}_k = \frac{\sum_{f=1}^{n} \alpha_f S_f}{\sum_{f=1}^{n} S_f} \tag{9}$$

where the subscripts k and f represents the cell and face indexes, respectively; S is the surface area. This smoothing procedure transforms the indicator function by interpolating it from cell centres to face centres back to the cell centres, which is repeated twice.

The equations are solved using standard numerical schemes (Gauss linear), except for the velocity component advection term and flux of the compression velocity. Furthermore, the advection equation for the volume fraction is solved using an explicit temporal solver with a first order spatial discretization scheme. The transient terms are discretized using a first order implicit Euler scheme and the *MULES* (Multidimensional Universal Limiter with Explicit Solution) explicit solver is used to ensure the boundedness of the phase fraction function. The *PIMPLE* (Pressure Implicit Method for Pressure Linked Equations) algorithm with 2 corrector loops and interface compression is applied for the pressure-velocity coupling to obtain a sharp interface.

The CFL condition was used to limit the time step, which is based on the maximum Courant number (Co) as indicated in Eq. (10).

$$\mathrm{Co} = \frac{|\vec{u}| \Delta t}{\Delta x} \tag{10}$$

where $|\vec{u}|$ is the magnitude of the velocity in the cell, Δt is the time-step, and Δx is the cell size in flow direction. For all considered cases, Co is limited to 0.5 in the bulk of the phases, and to 0.25 in the interfacial region.

The flow-focusing geometry was reconstructed using *SALOME-8.3.0* (SALOME, 2018) and the numerical mesh was generated with the *snappyHexMesh* utility. The entrance lengths (l_{ent}) were calculated in order to ensure fully developed flow, $l_{ent} = 0.379\mathrm{e}^{-0.148\mathrm{Re}} + 0.055\mathrm{Re} + 0.26$, as proposed by Dombrowski et al. (1993). A mesh independency study to achieve stable droplet size was performed, and the final mesh element sizes are $\Delta x_{c,x} = \Delta x_{c,y} = \Delta x_{c,z} = 25$ μm (*blockMesh* utility), with refinement layers near the walls but without grading. The final mesh consists of a total of 392 189 cells. Fig. 3 illustrates different planes of the discretized solution domain.

The thickness of the film developed between the droplet interface and the Teflon wall can be estimated using *Bretherton's law* (Bretherton, 1961), which is expressed in Eq. (11) for circular cross-sections and for low values of the Capillary number ($\mathrm{Ca_d} < 0.01$) (Baroud et al., 2010; Kurup and Basu, 2011).

$$e = 1.34 \frac{d_{\mathrm{t}}}{2} \left(\frac{u_{\mathrm{d}} \mu_{\mathrm{c}}}{\sigma} \right)^{2/3} \tag{11}$$

For our simulated conditions, the film thickness is situated in the range 1.2–1.7 μm. Our computational mesh is therefore not able to resolve the film. However, simulations performed by Raj et al. (2010) showed that for $\mathrm{Ca_c} < 0.01$ there is no film, and our simulated cases are in the same range of Capillary numbers.

2.3. Protein crystallization

During the crystallization experiments, the protein used was chicken egg white lysozyme (purchased from Merck CAS-No. 9001-63-2), without further purification. Lysozyme and precipitant agent aqueous solutions [sodium chloride 6% (w/v), obtained from Panreac AppliChem (99.5%, Germany)] were both prepared in a 0.2 M sodium acetate buffer stock solution [sodium acetate trihydrate from Sigma-Aldrich (99.5%, Germany)], whose pH was adjusted to 4.7 with glacial acetic acid [Merck (100%, Germany)]. Sodium chloride aqueous solution pH was posteriorly adjusted with a 1 M hydroxide sodium (Pronolab, Portugal) solution. All the solutions were prepared with ultrapure water (Milli Q water, resistivity of 18.3 MΩ·cm^{-1} at 20 °C) and filtered using syringe filters (Puradisc FP 30 mm, cellulose acetate, 0.2 μm [Sigma-Aldrich, Whatman, Germany]). Microbatch lysozyme crystallization trials were then carried out by mixing the lysozyme and sodium chloride aqueous solutions in a *T*-junction before the intersection between the continuous and the dispersed phases.

2.4. Phase diagram construction

A two-dimensional (2D) phase diagram, representing the protein concentration as a function of temperature, was determined to depict the metastability zone for the studied conditions: 3% (w/v) sodium chloride and pH 4.7. For this, microbatch crystallization assays were performed at different supersaturation levels by changing the initial lysozyme concentration ($C_{lysozyme} \in [12.5–57.5]$ mg·ml^{-1}) and the temperature ($T \in [10–25]$ °C). For all experiments, the droplet-based platform was filled with the silicon oil and both lysozyme and salt solutions as soon as the temperature in the droplet incubation zone reached steady state. This ensures that the crystallization assays were conducted at a defined constant temperature. Supersaturation was expressed by the ratio between the initial protein concentration in solution (C_0) and the protein solubility (C_s), as represented by Eq. (12) (Mullin, 2001; Giegé and McPherson, 2006; Ducruix and Giegé, 1999).

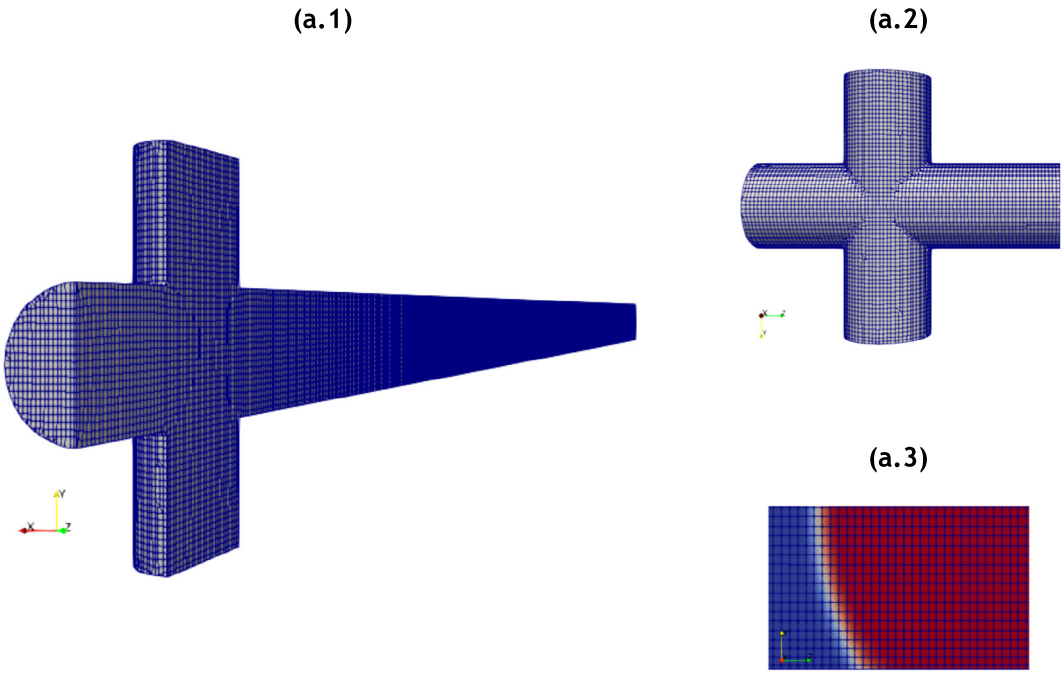

Fig. 3. Discretized solution domain (a.1) 3D view (middle plan *x*-*y*), (a.2) side view (*y*-*z*) of the microchannel entrances and (a.3) Computed droplet curvature by the VOF method in a 2D plane (*y*-*z*).

$$S = \frac{C_0}{C_s} \tag{12}$$

As previously mentioned, the lysozyme and salt solutions were mixed by a simple passive micromixer (*T*-junction) using equal flow rates. The droplets were then generated using another basic passive micromixer (flow-focusing junction) and silicon oil as the carrier fluid. It was necessary to wait a certain time to ensure droplet stability and monodispersity. At this moment, the syringe pumps were stopped, after which each generated droplet can be considered as an independent microreactor. After approximately 20 h, the droplets were observed using optical microscopy: the droplets were classified as belonging to the metastable, labile or precipitation zone and the crystals were counted. Afterwards, 3 independent microbatch trials were conducted for the hydrodynamic condition that allows the generation of the smallest droplet size.

2.5. Nucleation probability

Different methods to assess nucleation experiments by microscopy techniques are available (García-Ruiz, 2003). In this study, the applied method was based on the probability of nucleation events. Crystal nucleation is a stochastic mechanism and can be considered as an independent event from one droplet to another. The nucleation probability [Eq. (13)] is defined as the probability of finding at least a single crystal in a droplet (Bhamidi et al., 2017; Teychené and Biscans, 2011, 2012).

$$P_{nucl} = 1 - \frac{N_e}{N_t} \tag{13}$$

where N_e is the number of droplets that do not contain any crystal and N_t the total number of droplets. It was assumed that an event is included on the metastable zone if the nucleation probability was less than 10% ($P_{nucl} < 0.1$), which means a low nucleation probability. The obtained data led to the construction of a lysozyme phase diagram for static droplets generated in a single hydrodynamic condition.

3. Results and discussion

3.1. Hydrodynamic study

The hydrodynamic conditions in the present study, squeezing regime in a flow-focusing geometry, are characterized by low values of the Capillary number, $Ca_c < 0.1$ and $Ca_d < 0.01$ (Zhu and Wang, 2017). These ranges indicate that interfacial tension dominates over the viscous forces during the droplet breakup and formation, controlling the evolution of the interface (Baroud et al., 2010). In the VOF method, this effect is responsible for the generation of spurious currents (parasitic currents) that tend to appear near the interface and in the recirculation zones of the droplet. Fig. 4 depicts the velocity field streamlines inside and in the vicinity of the droplet interface in a reference frame moving with the droplet. The moving reference frame allows to visualize the secondary flow and resulting recirculate motions. At the lowest Capillary number, Ca_d (Case #1, Table 2), recirculation zones also appear outside the droplet, which are non-physical and are caused by afore mentioned spurious currents.

These unphysical velocity values are exclusively due to numerical inadequacies during the calculation of the interface curvature and normal vectors, which have a direct effect in the momentum equation for the calculation of the surface tension term. However, for all the cases, the droplet topology and curvature are apparently not affected by the spurious currents (Fig. 4). The magnitude of the spurious currents increases with decreasing Capillary number, which is also observed in Fig. 4(a.1).

Droplet generation in the squeezing regime resulted in uniform droplets in an extended range of droplet sizes with good frequency and monodispersity (see Fig. 5). Table 2 lists the experimental conditions of the performed experiments in terms of the flow rates of the continuous (Q_c) and dispersed (Q_d) phase, the flow rate ratio $\alpha_c = Q_c/(Q_c + Q_d)$, and the resulting Capillary numbers, calculated as expressed by Eq. (14).

$$Ca_i = \frac{u_i \mu_i}{\sigma} \tag{14}$$

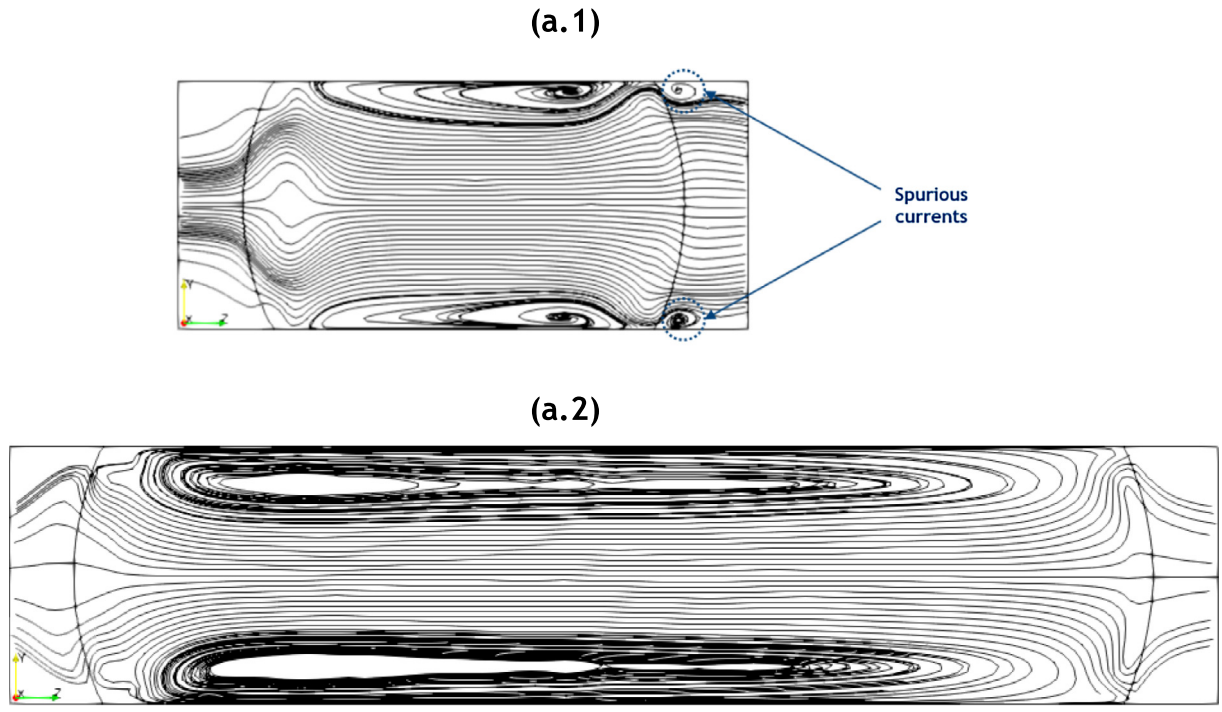

Fig. 4. Streamlines within the radial direction (moving droplet reference frame) in a 2D plane (y-z) for: (a.1) Case #1 and (a.2) Case #5. [Recirculate motions outside the droplet are caused by non-physical velocities.]

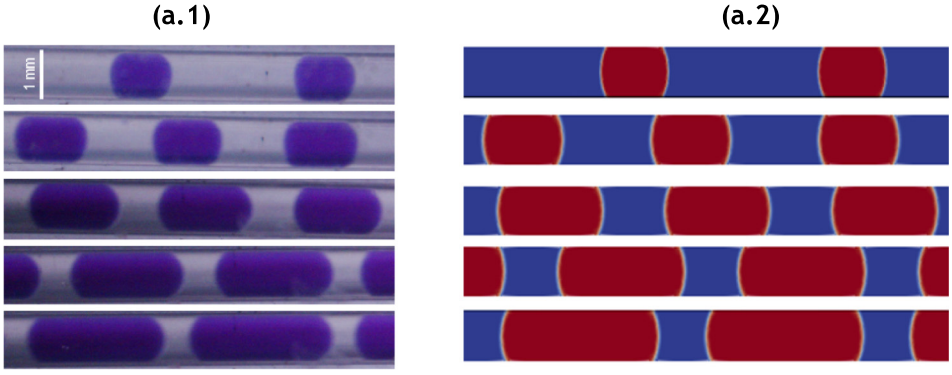

Fig. 5. Comparison between (a.1) experimental and (a.2) numerical (volume fraction) results obtained in a flow-focusing cylindrical geometry.

where u_i denotes the superficial velocity and μ_i the dynamic viscosity of each phase i (i = c for continuous phase or i = d for dispersed phase); σ is the interfacial tension.

In the hydrodynamic study we numerically predicted and experimentally measured the dispersed droplet size. Fig. 5 depicts a qualitative comparison of the droplet images obtained from experiments and the corresponding simulation results, while in Fig. 6 the normalized droplet length with the Teflon tube diameter is presented, where the numerically obtained results are averaged for the first 5 generated droplets, and the experimental results represent the average of around 750 droplets per experiment. A very good agreement between the experimental and numerical results is observed, which proves that the applied VOF model is capable of predicting the droplet generation in the flow-focusing geometry at low Capillary numbers. The only significant deviation is observed for the experimental point in the plug flow regime that corresponds to the highest Q_d, which also corresponds to the lowest Ca_c (Table 2). However, the experimentally observed droplet size distribution (Fig. 7) for this case is broader compared to the other conditions. Furthermore, for this fluid flow condition, the smallest separation between droplets is observed (Fig. 5), and consequently coalescence is more probable to occur. This effect might explain the shift to larger sizes compared to the numerically predicted droplet length for this fluid flow condition.

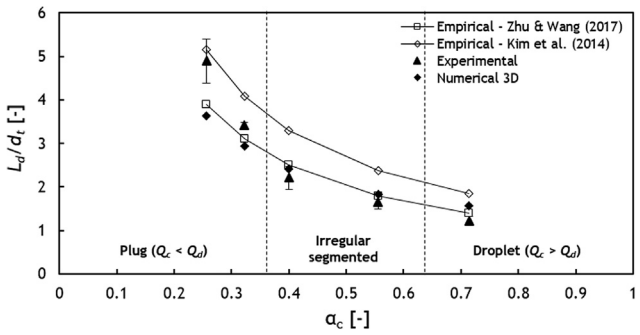

Fig. 6. Droplet length (L_d) normalized with the Teflon tube diameter (d_t) as a function of the flow rate ratio (α_c) in a flow-focusing geometry. Empirical scaling laws: $L_d/d_t = 1 + Q_d/Q_c$ (Zhu and Wang, 2017) and $L_d/d_t = 1.32/\alpha_c$ (Kim et al., 2014). [The error bars are standard deviations from 3 independent experiments].

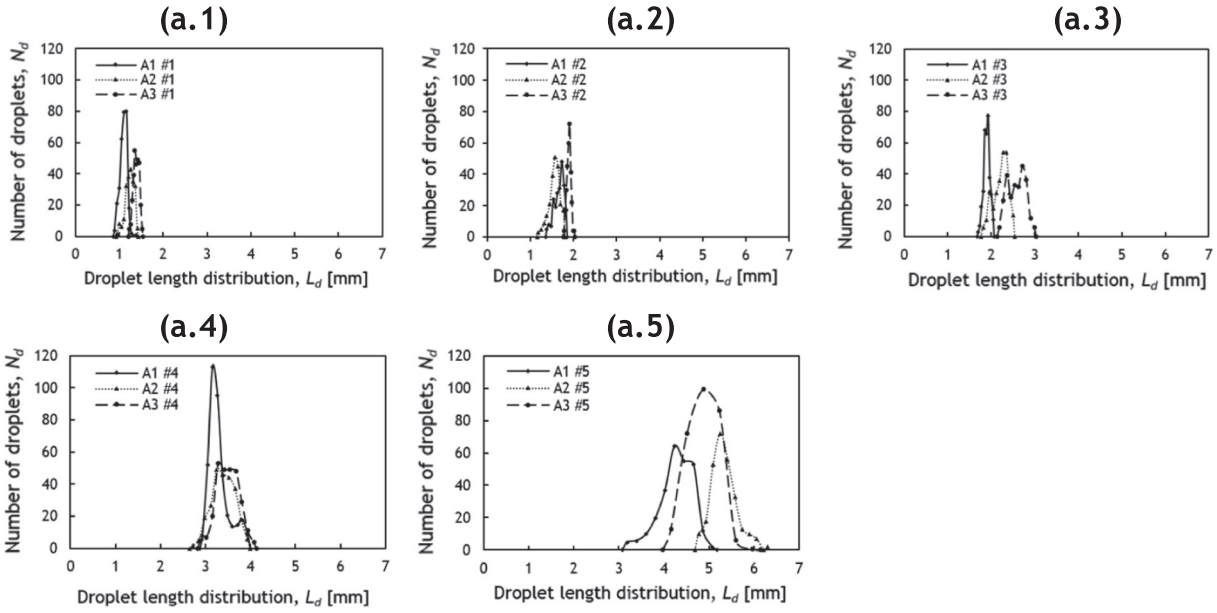

Fig. 7. Droplet size distribution: (a.1) Case #1, (a.2) Case #2, (a.3) Case #3, (a.4) Case #4, (a.5) Case #5. [Each assay was performed in triplicate].

A comparison of the experimentally and numerically obtained droplet sizes with empirical correlations from literature reveals a good agreement with the correlation reported by Zhu and Wang (2017), represented by open squares in Fig. 6.

$$L_d/d_t = 1 + Q_d/Q_c \tag{15}$$

Garstecki et al. (2006) reported that this correlation is limited to *T*-junction geometries. However, in the squeezing regime and at similar phase viscosities (Table 1), the mechanisms involved during the droplet generation could be considered identical for both hydrodynamic configurations. Furthermore, the empirical correlations are usually obtained for geometries with rectangular cross-sections, which can limit the applicability of the power laws (Baroud et al., 2010; Funfschilling et al., 2009) (Fig. 6). The typical form of a correlation to predict the droplet size in a *T*-junction is $L_d/d_t = k_1 + k_2 Q_d/Q_c$ (Garstecki et al., 2006). A proposed correlation to predict the droplet size in a flow-focusing geometry is of the form $L_d/d_t = k_3/\alpha_c$, e.g. with $k_3 = 1.32$ as suggested by Kim et al. (2014) (represented by open diamonds in Fig. 6). As this empirical correlation overpredicts the observed droplet size, a power law was used to fit the experimental results, which is shown in Fig. 8. This power law is able to predict the droplet sizes for all considered values of the continuous and dispersed phase flow rates.

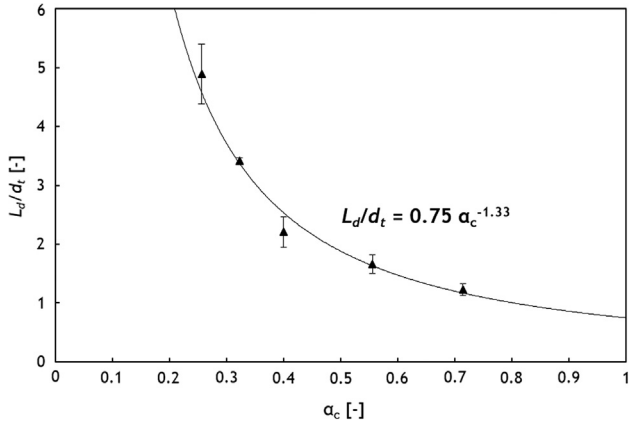

Fig. 8. Droplet length (L_d) normalized with the Teflon tube diameter (d_t) as a function of the flow rate ratio (α_c) in a flow-focusing geometry. The line represents a power law fit to the experimental results. [The error bars are standard deviations from 3 independent experiments.].

3.2. Phase diagram construction

Lysozyme (Lot no. K46535581 514) crystallization trials for the construction of a phase diagram were performed, which is crucial to quantify the range of initial protein concentration and temperature suitable for lysozyme crystallization in a droplet-based microreactor (Teflon tube) at sodium chloride 3% (w/v) and pH 4.7.

To obtain a reliable phase diagram, the formed droplets need to be monodisperse and stable. Indeed, the droplet volume plays an important role in the nucleation mechanism, an effect currently not sufficiently well understood in the scientific community (Hammadi et al., 2013). To construct the phase diagram, we chose the flow condition which results in the smallest droplets ($\alpha_c = 0.714$). However, small droplet volumes can lead to lower nucleation probability, as the number of available spots where nucleation can take place is lower and, consequently, the width of the metastable region could be larger. Thereby, this metastable region may include the metastability limits for the other droplet flow conditions, since the droplet volume is higher for the other hydrodynamic conditions. Fig. 9(a) represents all the experimental points, with the presence or absence (clear droplets) of crystals inside the droplets. The lysozyme phase diagram in the droplet-based microfluidic platform, representing the lysozyme concentration as a function of the temperature is plotted in Fig. 9(b).

The solubility line is entirely defined by thermodynamics, and can be described by the van't Hoff equation (Mullin, 2001) [Eq. (16)].

$$\Delta G^\circ = RT \ln K_{eq} \tag{16}$$

where ΔG° is the Gibbs free energy, K_{eq} the equilibrium constant, R the ideal gas constant, and T represents the absolute temperature. After substituting the Gibbs free energy with its enthalpic (ΔH°) and entropic (ΔS°) contributions, Eq. (17) is obtained.

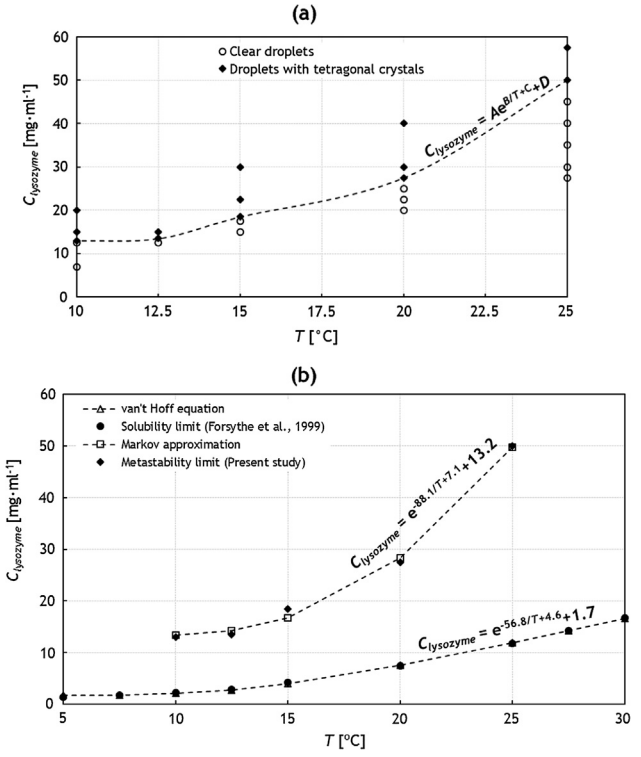

Fig. 9. Lysozyme phase diagram at sodium chloride 3% (w/v) and pH 4.7 in the droplet-based microfluidic platform: (a) The indicated correlation provides the best fit for the studied temperature range and (b) the indicated exponential fits were obtained using van't Hoff equation (solubility limit) and Markov approximation (metastability limit)].

$$\ln K_{eq} = \frac{\Delta H^{\circ}}{RT} - \frac{\Delta S^{\circ}}{R} \tag{17}$$

In this way, a theoretical equation to describe the solubility concentration (C_s) in function of temperature can be obtained [Eq. (18)]

$$C_s(T) = Ae^{B/T+C} + D \tag{18}$$

where the parameters A, B, C and D are determined through the minimization of the sum of quadratic errors between the theoretically calculated and experimentally obtained concentrations. The parameters B ($-\Delta H^{\circ}/R$) and C ($\Delta S^{\circ}/R$) allow the calculation of the system's enthalpy and entropy, respectively.

The metastability line is a virtual limit, which results from a combination of thermodynamics and kinetics, and the most important, the type of the crystallizer. Nucleation probability is defined by Eq. (19)

$$P_{nucl} = e^{-\Delta G^{*}/k_B T} \tag{19}$$

where ΔG^{*} is the critical Gibbs free energy and k_B is the Boltzmann constant. Analogously to the solubility limit, a theoretical equation to describe the metastability concentration (C_m) in function of temperature is obtained [Eq. (20)]

$$C_m(T) = A'e^{B'/T+C'} + D' \tag{20}$$

where the parameters are again determined through the minimization of the sum of quadratic errors. The parameter B' ($-\Delta G^{*}/k_B$) allows the calculation of the critical Gibbs free energy.

As previously mentioned, the solubility limit is well-defined and supported by a large number of published data for different conditions and system configurations. In this work, the solubility line was constructed based on data reported in literature by Forsythe et al. (1999). The obtained parameters for both solubility and metastability limits are indicated in Tables 3 and 4, respectively.

Table 3
Parameter values to predict the solubility limit using Eq. (18) in different case studies.

	Studied case	Ildefonso et al. (2012a)	Maosoongnern et al. (2012)	
pH	4.7	4.5	4.4	5
C_{NaCl} [% (w/v)]	3	4	3	3
V_d	0.9 μl	0.25 μl	4 ml	4 ml
A [mg·ml^{-1}]	1	1	1	1
B [°C]	−56.8	−129.7	−166.2	−168.3
C [–]	4.6	6.1	8.7	8.6
D [mg·ml^{-1}]	1.7	1.9	1.7	1.5
ΔH° [kJ·K^{-1}·mol^{-1}]	−129	−295	−379	−383
ΔS° [kJ·mol^{-1}]	−10	−14	−20	−20

Table 4
Parameter values to predict the metastability limit using Eq. (20) in different case studies.

	Studied case	Ildefonso et al. (2012a)	Maosoongnern et al. (2012)	
pH	4.7	4.5	4.4	5
[NaCl] [% (w/v)]	3	4	3	3
V_d	0.9 μl	0.25 μl	4 ml	4 ml
A′ [mg·ml^{-1}]	1	1	1	1
B′ [°C]	−88.1	−416.6	−18.0	−15.2
C′ [–]	7.1	15.2	4.5	4.3
D′ [mg·ml^{-1}]	13.2	13.9	24.6	25.8
ΔG^{*} [kJ·mol^{-1}]	0.73	3.5	0.14	0.12

Based on the obtained values, it can be concluded that for different pH values (data reported by Maosoongnern et al., 2012), the enthalpic and entropic values are similar. It is also worth noting that the change in entropy is similar for different set-up configurations, and operation at different flow rates, pH value and salt concentration. However, the enthalpic values depend on the used methodology and even at the same conditions different values could be obtained.

The higher Gibbs free energy values for the cases where the droplet volume is lower could be explained considering the nucleation barrier. For these cases, the higher critical activation free energy barrier could also confirm the difficulty to nucleate in microliter droplets (García-Ruiz, 2003), where the nucleation probability decreases.

As presented in Fig. 10, below the metastability limit, the solution is supersaturated but the critical supersaturation was not yet reached, and clear droplets are obtained. Nucleation should not occur (not spontaneously) and crystal growth is promoted. Otherwise, above the metastability limit, depending on the initial lysozyme concentration and temperature conditions (maintaining the initial salt concentration and pH value), tetragonal crystals were obtained varying in terms of number and size [Fig. 10(a)]. The values of initial supersaturation (S_i) and nucleation probability (P_{nucl}) are represented in Fig. 10(b).

With our set of experiments, we are able to clearly define the nucleation and metastable regions based on the nucleation probability [Fig. 10(b)]. In the metastable region, as explained above, the limit of nucleation probability was initially fixed at 10% (low nucleation probability), but for the studied conditions this probability value was always below 10%. In the labile region, where nucleation is spontaneous, the nucleation probability was higher than 80% for all the cases.

For all temperatures, a large number of small crystals was observed at the lowest investigated concentration level [Fig. 10

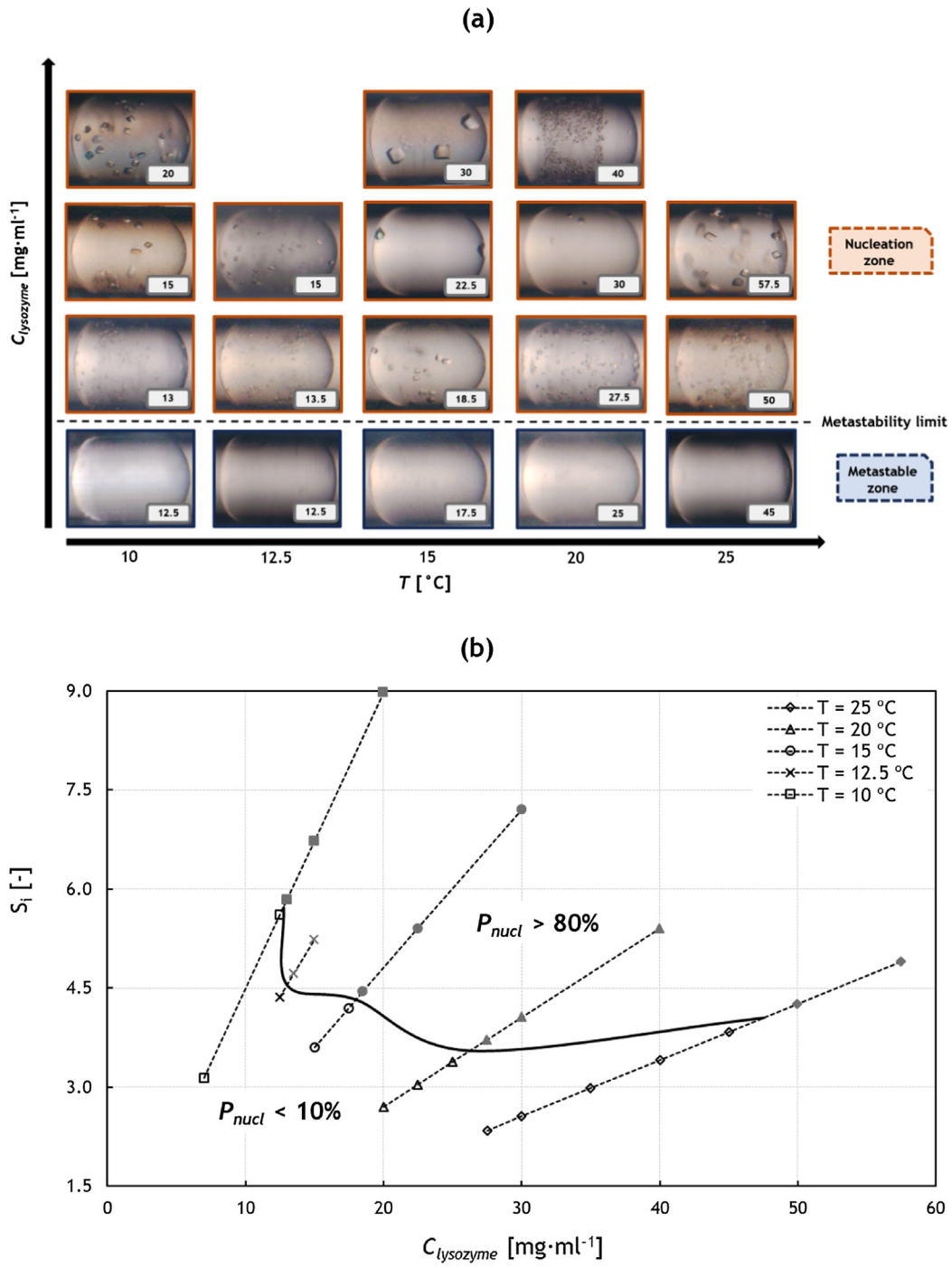

Fig. 10. (a) Lysozyme crystals obtained in the droplet-based microfluidic platform at sodium chloride 3% (w/v) and pH 4.7 [Lysozyme concentrations in mg·ml^{-1} are indicated in each picture, increasing along both abscissa and ordinates axes] with the indication of metastable and nucleation zones. (b) Initial supersaturation and nucleation probability values for the crystallization trials. [Clear markers correspond to clear droplets and grey markers to droplets with tetragonal crystals].

(a)]. At the same temperature, for a sequential increase in the supersaturation, an increase in crystal size was observed. In principle, this observation is not expected, since the formation of many small crystals is usually observed at higher supersaturations, and smaller crystals are expected for higher supersaturations (higher nucleation rate). A possible explanation for this observation could be increased crystal growth rates for larger crystal sizes, due to the increased supersaturation levels. Furthermore, for higher supersaturation values, it was also possible to identify preferential locations of crystal formation at the droplet interface. For the studied range of Capillary numbers, besides the dominance of the interfacial forces during the droplet formation, these observations can also indicate heterogeneous nucleation.

For the same supersaturation level (22.5 mg·ml^{-1} at 15 °C and 40 mg·ml^{-1} at 20 °C) [Fig. 10(b)], the number of crystals is higher for the droplets with higher initial lysozyme concentration [Fig. 10(a)]. For identical initial lysozyme concentrations (15 mg·ml^{-1} at 10 °C and 12.5 °C, and 30 mg·ml^{-1} at 15 °C and 20 °C in Fig. 10(a)), decreasing the temperature increases the crystal size, which is also observed when the temperature is maintained, and the concentration is gradually increased. For the latter, despite the increase in supersaturation level (enhancing nucleation), the

crystal size increases. However, there is an extreme value at 20 °C (40 mg·ml^{-1}), where possibly amorphous particles are present in large number. A possible explanation is the proximity to the precipitation zone (high supersaturation levels) in the phase diagram.

Due to nucleation in microliter volumes, it is expected that the nucleation probability is low, and the formation of a lower number of crystals could be expected for the entire range of temperatures and lysozyme concentrations, and not only for higher supersaturation levels (Hammadi et al., 2013; Grossier et al., 2011). A possible explanation for this unpredictable behaviour could be the presence of different states of lysozyme aggregation (oligomer formation) in solution and their implications on the occurrence of nucleation. Ferreira et al. (2017) reported the effect of lysozyme concentration on the oligomer concentrations for a specified range of experimental conditions ($T \in$ [12.5–20] °C and $C_{lysozyme} \in$ [25–50] mg·ml^{-1}), which includes the labile zone for the studied case at T = 20 °C. At T = 15 °C, Ferreira and co-workers observed a gradual increase in the oligomer concentration with the lysozyme concentration, but a decrease in monomer concentration was observed for the highest lysozyme concentration. This observation emphasizes the complex behaviour of lysozyme in solution and the possible implications on nucleation and crystal growth, since nucleation will be difficult to achieve due to the lower availability of monomers. The results could be explained as a competition between cluster growth (oligomers can act as heterogeneous nucleation sites) and crystal growth (Ferreira et al., 2017; Price et al., 1999). For the entire temperature range, the oligomer presence should promote crystal growth and this point could explain the formation of few large crystals at higher supersaturation levels. However, the final crystal size is different at different temperatures. On the one hand, there is the concentration effect, where higher supersaturations should result in smaller crystals. On the other hand, there is the behaviour of the oligomeric solution, which changes depending on temperature.

Based on the fact that the images shown in Fig. 10(a) were taken at the end of the experiments, intermediate stages during nucleation and crystals growth were not represented. The crystal size distribution appears to be uniform, which could be explained by Ostwald ripening (Vetter et al., 2013). This mass transport process is responsible for an increase in the mean crystals radius increase over time due to lysozyme diffusion from smaller to larger crystals (Streets and Quake, 2010).

Another observation is the absence of crystals in the droplet caps at 20 °C and 40 mg·ml^{-1}. This could be explained by asymmetrical mixing patters due to heterogeneous local concentrations inside the droplet. During the droplet formation, besides diffusion there is also convection contributing to mixing. The convection contribution ($u_d L_d$) is 1.7 × 10^{-7} m^2·s^{-1}, while the diffusion coefficients of lysozyme and sodium chloride at 20 °C are 1.4 × 10^{-10} m^2·s^{-1} and 2.0 × 10^{-9} m^2·s^{-1}, respectively (Howard et al., 2009). However, when the droplets are stopped (microbatch experiments), mixing may predominantly occur by molecular diffusion.

Crespo et al. (2010) and Castro et al. (2016) reported studies with the same nature and concentration of precipitant agent and buffer, and pH value at 20 °C, but for different geometries and mixing behaviour. In the present work, the lysozyme concentration in the metastability limit is 27.5 mg·ml^{-1}, and as previously mentioned each droplet has a volume of 0.9 μl. Crespo et al. (2010) performed batch lysozyme trials in microwells under static conditions in droplets with a volume of 8 μl. In this case, the lysozyme concentration in the metastability limit is 29.5 mg·ml^{-1}. The small reduction of the lysozyme concentration in the metastable zone for the studied case compared to the one conducted by Crespo et al. (2010) can be explained by the influence of convection during droplet generation, or even due to an interfacial effect (lower surface to volume ratio). However, due to the result uncertainty, this difference is not statistically significant. Castro et al. (2016) conducted batch lysozyme trials under dynamic conditions using an oscillatory flow mixing within a volume of 4 ml. In this case, the lysozyme concentration in the metastability limit is 23.1 mg·ml^{-1}. It is possible to observe nucleation at a lower lysozyme concentration, and the metastability zone width apparently decreases, which was expected as besides molecular diffusion, (oscillatory) convection also significantly contributes to mixing. Apparently, the crystal morphology is identical in all the cases (tetragonal crystals), but their number and sizes are different. Besides that, it was reported by Wang et al. (2008) that for temperatures lower than 25 °C, lysozyme crystals are tetragonal.

4. Conclusions

This work introduces a rational and systematic screening strategy to address the highly variable nature of protein crystallization. The developed droplet-based microfluidic platform enables the production of uniform and stable droplets with a very good frequency (up to 250 droplets per assay). It also allows a large flexibility regarding the generated droplet volume (range of 0.9–18 μl). The numerical simulations were validated by experimental measurements and empirical data. Furthermore, this numerical approach accurately predicts the droplet curvature and the complex flow topology effects inside the droplets, with a significant suppression of the artificial spurious velocities at the interface. However, the impact of the artificial velocities on the simulations increases for low Capillary numbers. Approaches for further suppression should be explored in more detail, especially for simulations of coupled interfacial heat and mass transfer.

The construction of the lysozyme phase diagram allowed the calculation of the thermodynamic and kinetic parameters based on the experimental data and further comparisons with reported systems in literature. It was possible to conclude that the droplet volume has a major contribution to the nucleation probability. It was theoretically expected that in droplet-based microfluidics, the nucleation probability decreases. Based on this, the formation of a lower number of crystals could be expected for the entire range of temperature and lysozyme concentration. This was however not observed due to the complex and stochastic mechanism of nucleation, including a possible competition between monomers and oligomers in solution.

Acknowledgements

S.K. acknowledges funding from the European Research Council under the ERC Starting Grant Agreement no. 677169–MicroParticleControl. F.C acknowledges FCT (postdoctoral fellowship [SFRH/BPD/96132/2013]) under the project POCI-01-0145-FEDER-006939 (Laboratory for Process Engineering, Environment, Biotechnology and Energy – UID/EQU/00511/2013) funded by the European Regional Development Fund (ERDF), through COMPETE2020 – Programa Operacional Competitividade e Internacionalização (POCI) and by national funds, through FCT – Fundação para a Ciência e a Tecnologia. We thank OpenFoam developers and contributors for the use of their codes, especially Kevin van As from the Transport Phenomena Group (TU Delft). We also thank Vahid Kazemi Kamyab, Milad Mottaghi and Khurram Shazad for all the suggestions and discussions on the simulations.

References

Akella, S.V., Mowitz, A., Heymann, M., Fraden, S., 2014. Emulsion-based technique to measure protein crystal nucleation rates of lysozyme. Cryst. Growth Des. 14 (9), 4487–4509.

Anna, S.L., 2016. Droplets and bubbles in microfluidic devices. Annu. Rev. Fluid Mech. 48 (1), 285–309.

Baroud, C.N., Gallaire, F., Dangla, R., 2010. Dynamics of microfluidic droplets. Lab Chip 10 (16), 2032.

Belkadi, A., Tarlet, D., Montillet, A., Bellettre, J., Massoli, P., 2015. Water-in-oil emulsification in a microfluidic impinging flow at high capillary numbers. Int. J. Multiph. Flow 72, 11–23.

Bhamidi, V., Kenis, P.J.A., Zukoski, C.F., 2017. Probability of nucleation in a metastable zone: induction supersaturation and implications. Cryst. Growth Des. 17, 1132–1145.

Brackbill, J.U., Kothe, D.B., Zemach, C., 1992. A continuum method for modeling surface tension. J. Comput. Phys. 100 (2), 335–354.

Bretherton, F.P., 1961. The motion of long bubbles in tubes. J. Fluid Mech. 10 (2), 166–188.

Castro, F., Ferreira, A., Teixeira, J., Rocha, F., 2016. Protein crystallization as a process step in a novel meso oscillatory flow reactor: study of lysozyme phase behavior. Cryst. Growth Des., 1–8

Chayen, N.E., Saridakis, E., 2008. Protein crystallization: from purified protein to diffraction-quality crystal. Nat. – Methods 5, 147–153.

Crespo, R., Martins, P.M., Gales, L., Rocha, F., Damas, A.M., 2010. Potential use of ultrasound to promote protein crystallization. J. Appl. Crystallogr. 43 (6), 1419–1425.

Dhouib, K., Khan Malek, C., Pfleging, W., Gauthier-Manuel, B., Duffait, R., Thuillier, G., Ferrigno, R., Jacquamet, L., Ohana, J., Ferrer, J.-L., Théobald-Dietrich, A., Giegé, R., Lorber, B., Sauter, C., 2009. Microfluidic chips for the crystallization of biomacromolecules by counter-diffusion and on-chip crystal X-ray analysis. Lab Chip 9 (10), 1412–1421.

Dombrowski, N., Foumeny, E.A., Ookawara, S., Riza, A., 1993. The influence of Reynolds number on the entry length and pressure drop for laminar pipe flow. Can. J. Chem. Eng. 71 (3), 472–476.

Ducruix, A., Giegé, R., 1999. Crystallization of Nucleic Acids and Proteins: A Practical Approach. Oxford University Press.

Ferreira, C., Barbos, S., Taboada, P., Rocha, F.A., Damas, A.M., Martins, P.M., 2017. The nucleation of protein crystals as a race against time with on- and off-pathways. J. Appl. Crystallogr. 50, 1056–1065.

Ferreira, A., Faria, N., Rocha, F., Teixeira, J., 2011. Using an online image analysis technique to characterize sucrose crystal morphology during a crystallization run. Ind. Eng. Chem. Res., 6990–7002

Ferreira, A., Pereira, G., Teixeira, J.A., Rocha, F., 2012. Statistical tool combined with image analysis to characterize hydrodynamics and mass transfer in a bubble column. Chem. Eng. J. 180, 216–228.

Forsythe, E.L., Judge, R.A., Pusey, M.L., 999. Tetragonal chicken egg white lysozyme solubility in sodium chloride solutions. J. Chem. Eng. Data 44 (3), 637–640.

Funfschilling, D., Debas, H., Li, H.Z., Mason, T.G., 2009. Flow-field dynamics during droplet formation by dripping in hydrodynamic-focusing microfluidics. Phys. Rev. E – Stat. Nonlinear Soft Matter Phys. 80 (1), 2–5.

García-Ruiz, J.M., 2003. Nucleation of protein crystals. J. Struct. Biol. 142 (1), 22–31.

Garstecki, P., Fuerstman, M.J., Stone, H.A., Whitesides, G.M., 2006. Formation of droplets and bubbles in a microfluidic T-junction-scaling and mechanism of break-up. Lab Chip 6 (3), 437–446.

Gerdts, C.J., Tereshko, V., Yadav, M.K., Dementieva, I., Collart, F., Joachimiak, A., Stevens, R.C., Kuhn, P., Kossiakoff, A., Ismagilov, R.F., 2006. Time-controlled microfluidic seeding in nL-volume droplets to separate nucleation and growth stages of protein crystallization. Angew. Chem. – Int. Ed. 45, 8156–8160.

Giegé, R., 2013. A historical perspective on protein crystallization from 1840 to the present day. FEBS J. 280 (24), 6456–6497.

Giegé, R., McPherson, A., 2006. Chapter: crystallization – general methods. In: Arnold, E., Himmel, D.M., Rossmann, M.G. (Eds.), International Tables of Crystallography, Vol. F, Crystallography of Biological Macromolecules, second ed. John Wiley & Sons, pp. 81–93.

Grossier, R., Hammadi, Z., Morin, R., Veesler, S., 2011. Predictive nucleation of crystals in small volumes and its consequences. Phys. Rev. Lett. 107 (2), 1–4.

Günther, A., Jensen, K.F., 2006. Multiphase microfluidics: from flow characteristics to chemical and materials synthesis. Lab Chip 6 (12), 1487–1503.

Haeberle, S., Zengerle, R., 2007. Microfluidic platforms for lab-on-a-chip applications. Lab Chip 7, 1094–1110.

Hammadi, Z., Candoni, N., Grossier, R., Ildefonso, M., Morin, R., Veesler, S., 2013. Small-volume nucleation. Comptes Rendus Phys. 14 (2–3), 192–198.

Hamon, M., Hong, J.W., 2013. Systematic evaluation of the efficiencies of proteins and chemicals in pharmaceutical applications. In: Demirci, U., Khademhosseini, A., Langer, R., Blander, J. (Eds.), Microfluidic Technologies for Human Health, pp. 21–46.

Hoang, D.A., van Steijn, V., Portela, L.M., Kreutzer, M.T., Kleijn, C.R., 2013. Benchmark numerical simulations of segmented two-phase flows in microchannels using the Volume of Fluid method. Comput. Fluids 86, 28–36.

Hoang, D.A., van Steijn, V., Portela, L.M., Kreutzer, M.T., Kleijn, C.R., 2013. Benchmark numerical simulations of segmented two-phase flows in microchannels using the Volume of Fluid method. Comput. Fluids 86, 28–36.

Howard, E.I., Fernandez, J.M., Garcia-Ruiz, J.M., 2009. On the mixing of protein crystallization cocktails. Cryst. Growth Des. 9 (6), 2707–2712.

Howard, S.B., Twigg, P.J., Baird, J.K., Meehan, E.J., 1988. The solubility of hen egg-white lysozyme. J. Cryst. Growth 90, 94–104.

Ildefonso, M., Candoni, N., Veesler, S., 2011. Using microfluidics for fast, accurate measurement of lysozyme nucleation kinetics. Cryst. Growth Des. 11 (5), 1527–1530.

Ildefonso, M., Candoni, N., Veesler, S., 2012b. A cheap, easy microfluidic crystallization device ensuring universal solvent compatibility. Org. Process Res. Dev. 16 (4), 556–560.

Ildefonso, M., Revalor, E., Punniam, P., Salmon, J.B., Candoni, N., Veesler, S., 2012a. Nucleation and polymorphism explored via an easy-to-use microfluidic tool. J. Cryst. Growth 342 (1), 9–12.

Kim, N., Murphy, M.C., Soper, S.A., Nikitopoulos, D.E., 2014. Liquid-liquid segmented flows in polycarbonate microchannels with cross-sectional expansions. Int. J. Multiph. Flow 58, 83–96.

Kirby, B.J., 2010. Micro- and Nanoscale Fluid Mechanics: Transport in Microfluidic Devices. Cambridge University Press, Cambridge.

Kurup, G.K., Basu, A.S., 2011. Shape dependent Laplace vortices in deformed liquid-liquid slug flow. In: Proceedings of the Annual International Conference of the IEEE Engineering in Medicine and Biology Society, EMBS, pp. 4034–4037.

Lafaurie, B., Nardone, C., Scardovelli, R., Zaleski, S., Zanetti, G., 1994. Modelling merging and fragmentation in multiphase flows with SURFER. J. Comput. Phys. 113 (1), 134–147.

Leng, J., Salmon, J.-B., 2009. Microfluidic crystallization. Lab Chip 9 (1), 24–34.

Li, L., Ismagilov, R.F., 2010. Protein crystallization using microfluidic technologies based on valves, droplets, and slipchip. In: Annual Review of Biophysics, Buffalo., vol. 39, New York, pp. 139–158.

Li, Y., Reddy, R.K., Kumar, C.S.S.R., Nandakumar, K., 2014. Computational investigations of the mixing performance inside liquid slugs generated by a microfluidic T-junction. Biomicrofluidics 8 (5), 1–18.

Maeki, M., Yamaguchi, H., Tokeshi, M., Miyazaki, M., 2016. Microfluidic approaches for protein crystal structure analysis. Anal. Sci. 32, 3–9.

Maosoongnern, S., Diaz Borbon, V., Flood, A.E., Ulrich, J., 2012. Introducing a fast method to determine the solubility and metastable zone width for proteins: case study lysozyme. Ind. Eng. Chem. Res. 51 (46), 15251–15257.

Mullin, J.W., 2001. Crystallization. Oxford.

NIS Elements Basic Research – Microscope Imaging Software, 2017. [Online]. Available: <https://www.nikoninstruments.com/en_EU/Products/Software/NIS-Elements-Basic-Research> (accessed: March-2017).

Ngo, T.-D., Joo, SangWoo, Dang, Ich-Long, Byon, C., 2015. A numerical study on the dynamics of droplet formation in a microfluidic double T-junction. Biomicrofluidics 9, 1–14.

Nie, Z., Seo, M., Xu, S., Lewis, P.C., Mok, M., Kumacheva, E., Whitesides, G.M., Garstecki, P., Stone, H.A., 2008. Emulsification in a microfluidic flow-focusing device: effect of the viscosities of the liquids. Microfluid. Nanofluid. 5 (5), 585–594.

Nieves-Remacha, M.J., Yang, L., Jensen, K.F., 2015. OpenFOAM computational fluid dynamic simulations of two-phase flow and mass transfer in an advanced-flow reactor. Ind. Eng. Chem. Res. 54, 6649–6659.

Price, W.S., Tsuchiya, F., Arata, Y., 1999. Lysozyme aggregation and solution properties studied using PGSE NMR diffusion measurements. J. Am. Chem. Soc. 121 (49), 11503–11512.

Raj, R., Mathur, N., Buwa, V.V., 2010. Numerical simulations of liquid-liquid flows in microchannels. Ind. Eng. Chem. Res. 49 (21), 10606–10614.

Revalor, E., Hammadi, Z., Astier, J.P., Grossier, R., Garcia, E., Hoff, C., Furuta, K., Okustu, T., Morin, R., Veesler, S., 2010. Usual and unusual crystallization from solution. J. Cryst. Growth 312 (7), 939–946.

Roberts, M.M., Heng, J.Y.Y., Williams, D.R., 2010. Protein crystallization by forced flow through glass capillaries: enhanced lysozyme crystal growth. Cryst. Growth Des. 10 (3), 1074–1083.

"SALOME – The Open Source Integration Platform for Numerical Simulation," 2018. [Online]. Available: <http://www.salome-platform.org/> (accessed: February-2018).

Schieferstein, J.M., Pawate, A.S., Varel, M.J., Guha, S., Astrauskaite, I., Gennis, R.B., Kenis, P.J.A., 2018. X-ray transparent microfluidic platforms for membrane protein crystallization with microseeds. Lab Chip 18, 944–954.

Shi, H., Xiao, Y., Ferguson, S., Huang, X., Wang, N., Hao, H., 2017. Progress of crystallization in microfluidic devices. Lab Chip 23, 806–812.

Shui, L., Eijkel, J.C.T., van den Berg, A., 2007. Multiphase flow in microfluidic systems – control and applications of droplets and interfaces. Adv. Colloid Interface Sci. 133, 35–49.

Squires, T.M., Quake, S.R., 2005. Microfluidics: fluid physics at the nanoliter scale. Rev. Mod. Phys. 77 (3), 977–1026.

Streets, A.A., Quake, S.R., 2010. Ostwald ripening of clusters during protein crystallization. Phys. Rev. Lett. 104 (17), 1–9.

Tabeling, P., 2005. Introduction to Microfluidics. Oxford University Press, Paris.

Teh, S.-Y., Lin, R., Hung, L.-H., Lee, A.P., 2008. Droplet microfluidics. Lab Chip 8 (2), 198–220.

Teychené, S., Biscans, B., 2011. Microfluidic device for the crystallization of organic molecules in organic solvents. Cryst. Growth Des. 11 (11), 4810–4818.

Teychené, S., Biscans, B., 2012. Crystal nucleation in a droplet based microfluidic crystallizer. Chem. Eng. Sci. 77, 242–248.

van As, K., 2017. OF-kva_interfaceProperties [Online]. Available: <https://github.com/floquation/OF-kva_interfaceProperties> (accessed: February-2018).

Vetter, T., Iggland, M., Ochsenbein, D.R., Hänseler, F.S., Mazzotti, M., 2013. Modeling nucleation, growth, and ostwald ripening in crystallization processes: a comparison between population balance and kinetic rate equation. Cryst. Growth Des. 13 (11), 4890–4905.

Vorontsova, M.A., Maes, D., Vekilov, P.G., 2015. Recent advances in the understanding of two-step nucleation of protein crystals. Faraday Discuss. 179 (27), 27–40.

Walsh, G., 2015. Proteins: Biochemistry and Biotechnology. Wiley.
Wang, W., Shao, T., Zhao, S., Jin, Y., Cheng, Y., 2013. Experimental and numerical study of mixing behavior inside droplets in microchannels. Am. Inst. Chem. Eng. J. 59 (5), 1801–1813.
Wang, L.B., Wakayama, N.I., Tao, W.Q., 2008. The role of solutal convection in protein crystal growth – a new dimensionless number to evaluate the effects of convection on protein crystal growth. J. Cryst. Growth 310 (24), 5370–5374.
Wang, J., Wang, J., Feng, L., Lin, T., 2015. Fluid mixing in droplet-based microfluidics with a serpentine microchannel. RSC Adv. 5, 104138–104144.
Weller, H., 2017. OpenFOAM-5.x [Online]. Available: <https://github.com/OpenFOAM/OpenFOAM-5.x> (accessed: February-2018).
Whitesides, G.M., 2006. The origins and the future of microfluidics. Nature 442 (7101), 368–373.
Wörner, M., 2012. Numerical modeling of multiphase flows in microfluidics and micro process engineering: a review of methods and applications. Microfluid. Nanofluid. 12 (6), 841–886.
Yamaguchi, H., Maeki, M., Yamashita, K., Nakamura, H., Miyazaki, M., Maeda, H., 2013. Controlling one protein crystal growth by droplet-based microfluidic system. J. Biochem. 153 (4), 339–346.
Yang, C.-G., Xu, Z.-R., Wang, J.-H., 2010. Manipulation of droplets in microfluidic systems. Trends Anal. Chem. 29 (2), 141–157.
Zhang, S., Guivier-Curien, C., Vessler, S., Candoni, N., 2015a. Prediction of sizes and frequencies of nanoliter-sized droplets in cylindrical T-junction microfluidics. Chem. Eng. Sci. 138, 128–139.
Zhang, S., Ferté, N., Candoni, N., Veesler, S., 2015b. Versatile microfluidic approach to crystallization. Org. Process Res. Dev. 19 (12), 1–5.
Zhang, S., Gerard, C., Ikni, A., Ferry, G., Vuillard, L., Boutin, J., Ferte, N., Grossier, R., Candoni, N., Vessler, S., 2017a. Microfluidic platform for optimization of crystallization conditions. J. Cryst. Growth, 1–21.
Zhang, J., Wang, K., Teixeira, A.R., Jensen, K.F., Luo, G., 2017b. Design and scaling up of microchemical systems: a review. Annu. Rev. Chem. Biomol. Engi. 8 (1), 285–305.
Zheng, B., Tice, J.D., Roach, L.S., Ismagilov, R.F., 2004. A droplet-based, composite PDMS/glass capillary microfluidic system for evaluating protein crystallization conditions by microbatch and vapor-diffusion methods with on-chip X-ray diffraction. Angew. Chem. – Int. Ed. 43, 2508–2511.
Zheng, B., Gerdts, C.J., Ismagilov, R.F., 2005. Using nanoliter plugs in microfluidics to facilitate and understand protein crystallization. Curr. Opin. Struct. Biol. 15 (5), 548–555.
Zhu, P., Wang, L., 2017. Passive and active droplet generation with microfluidics: a review. Lab Chip 17 (1), 34–75.
Zhu, P., Wang, L., 2017. Passive and active droplet generation with microfluidics: a review. Lab Chip 17, 34–75.